J Mater Sci: Mater Electron (2018) 29:2275–2281
DOI 10.1007/s10854-017-8143-4

The structure, defects, electrical and magnetic properties of $BiFe_{1-x}Zr_xO_3$ multiferroic ceramics

H. Y. Dai[1] · L. T. Gu[1] · X. Y. Xie[1] · T. Li[1] · Z. P. Chen[1] · Z. J. Li[1]

Received: 28 September 2017 / Accepted: 24 October 2017 / Published online: 28 October 2017

Abstract $BiFe_{1-x}Zr_xO_3$ ($x = 0.00$–0.30) ceramics were synthesized using solid state reaction method followed by rapid liquid phase sintering, and the microstructure, electrical and magnetic properties of the synthesized ceramics were systematically investigated. The XRD patterns show that no impurity phases exist in Zr doped samples; Zr doping induces the crystal structure distortion when $x \leq 0.10$, and a structural phase transition occurs when the content of Zr varies from 0.10 to 0.20. SEM observations indicate that the average grain size is remarkably decreased by Zr doping. Positron annihilation lifetime spectra results indicate that cation vacancy-type defects exist in all samples, the cation vacancy concentration increases with increasing Zr content from 0.00 to 0.20, and then decreases with further increase of Zr content. Electrical and magnetic measurements show that enhanced leakage, ferroelectric and magnetic properties are observed in Zr doped ceramics. The analysis of microstructure and properties show that the cation vacancy defect plays an important role in modulating the electrical and magnetic properties of $BiFeO_3$.

1 Introduction

Multiferroic materials that simultaneously exhibit ferroelectric, (anti)ferromagnetic, and ferroelastic orderings within a single phase have attracted much attention recently due to their potential applications as well as interesting fundamental physics [1, 2]. Among the single-phase multiferroic materials, $BiFeO_3$ (BFO) with a rhombohedral perovskite structure is the most intensively studied material because it is the only single phase material which exhibits multiferroic properties at room temperature (with Curie temperature Tc ~ 1103 K and Neel temperature Tn ~ 643K) [3, 4]. Though these properties are very promising for the practical applications, BFO has some inherent problems including preparation of the pure phase compound, high leakage current, weak ferromagnetism and low magnetoelectric coupling coefficient [5, 6]. The high leakage current in BFO is attributed to the impurity phases, Fe^{2+} ions and oxygen vacancies resulting from the volatilization of Bi_2O_3 during high temperature sintering process. The magnetic ordering in BFO is an antiferromagnetic type, having a spatially modulated spin structure that does not allow net magnetization and inhibits observation of the linear magnetoelectric effect [5, 6]. These problems greatly prevent the practical applications of bulk BFO to multifunctional devices.

To overcome these problems, considerable attempts have been made [7–9] such as adopting various processing technique, oxygen ion implantation, epitaxial film growth, chemical leaching, application of large magnetic field, partial A-site/B-site cation substitution, making solid solutions with other perovskite materials, synthesizing BFO nanoparticles with grain size below 62 nm, and so on [7–9]. The method of cation substitution either at A-site, B-site, or A–B-sites is widely adopted due to its simplicity, good controllability, and effective enhancement in multiferroic properties of BFO. Rare earth elements such as La, Ce, Eu etc. or alkaline earth metal elements like Ba, Ca, Sr etc., have been substituted at A-site whereas transition metal elements such as Mn, Co, Ti, Zn etc., have been substituted at B-site [7–11]. It is found among those species that aliovalent ions with non-magnetic such as Zr^{4+}, which have a similar ion size with Fe^{3+}, seem especially attractive [12]. In addition, the

✉ Z. P. Chen
zhenpchen@163.com

[1] School of Physics and Electronic Engineering, Zhengzhou University of Light Industry, Zhengzhou 450002, China

substitution of Zr^{4+} for Fe^{3+} in BFO requires charge compensation, leading to the filling of oxygen vacancies, the formation of Fe^{2+} and/or the creation of cation vacancies [13]. Consequently, the multiferroic properties of BFO can be influenced greatly by Zr doping. However, the related published papers show that the effect of Zr doping on the microstructure and properties of the BFO seems very ambiguous [13–19]. It is well known that vacancy-type defects play a significant role in the properties of perovskite oxide [20]. Therefore, the investigation of the vacancy-type defects in perovskite oxide not only helps to understand the origin of physical properties but also has considerable technological significance. Positron annihilation spectroscopy (PAS) is a powerful method to study the atomic-scaled vacancy defects in materials [21–25]. Positrons are trapped preferentially by vacancy defects where electron density is lower than the bulk of material. Therefore, the annihilation characteristics of positrons are different in the perfect bulk state and vacancy trapped state, which makes the identification of vacancies very straightforward. In addition, PAS can offer the electrons density, defect type and defect concentration in materials qualitatively. In this paper, PAS is used to check the defects in BFO system, which few reports mentioned up to now. The related structural, electrical and magnetic properties of $BiFe_{1-x}Zr_xO_3$ along with the correlation between microstructure and electrical/magnetic properties were also investigated.

2 Experimental details

$BiFe_{1-x}Zr_xO_3$ ($x = 0.00$, 0.05, 0.10, 0.20 and 0.30) polycrystalline compounds were synthesized using solid state reaction method followed by rapid liquid phase sintering. High purity analytical powders of Bi_2O_3 (99.999%), Fe_2O_3 (99.99%) and ZrO_2 (99.99%) were exactly weighed according to the stoichiometric ratio with 3% excess of Bi_2O_3 for compensation of Bi loss. The starting powders were thoroughly ground in an agate mortar for 6 h using ethanol as a medium. The mixed powders were dehydrated at 150 °C for 12 h and dry pressed into small discs with 11 mm in diameter and 1.5 mm in thickness at 10 MPa pressure. The disks were sintered at 850–880 °C for 30 min and quenched subsequently to room temperature. To measure the electrical properties of the samples, the disks were carefully polished and coated with silver paste on both sides as electrodes, and then fired at 600 °C for 30 min.

The structures of the prepared samples were studied by Bruke D8 X-ray diffraction (XRD) with Cu-Kα radiation. The morphologies of the samples were observed by scanning electron microscopy (SEM, FEI Quanta200). The positron annihilation lifetime spectra were measured using a fast–fast coincidence lifetime spectrometer. A ^{22}Na positron source with intensity of about 13 μ Ci was used. The positron source was sandwiched between two identical pieces of samples for the positron lifetime measurements. Each spectrum contained a total of 10^6 counts. All the lifetime spectra were analyzed by PATFIT program. The leakage current and ferroelectric properties of all ceramics were measured using a RT 6000 ferroelectric tester. Magnetization versus applied magnetic field (M-H) data were collected in applied magnetic fields of up to 70 kOe using a Quantum Design vibrating-sample magnetometer (VSM). All these measurements were carried out at room temperature.

3 Results and discussion

Figure 1 presents the XRD patterns for the $BiFe_{1-x}Zr_xO_3$ ($x = 0.00$, 0.05, 0.10, 0.20 and 0.30) compositions measured at room temperature. Clearly, sharp and well-defined XRD patterns reveal a well crystallinity. The main peaks in XRD patterns of undoped BFO can be indexed by the distorted rhombohedral perovskite structure (with space group R3c). A very small amount of impurity phases such as $Bi_2Fe_4O_9$ and $Bi_{25}FeO_{40}$ (indicated by an asterisk in Fig. 1) appear in the XRD pattern of undoped BFO. This is often observed in the BFO ceramics synthesized by different methods [26, 27]. The occurrence of these impurity phases is unavoidable during the kinetics of BFO formation due to the volatilization of Bi atoms. However, it is found that there are no impurity phases can be observed in the XRD patterns of Zr doped samples, indicating that the substitution of B-site in BFO with Zr^{4+} ions yields single phases and suppresses the formation of the impurity phases. It should be noticed that with increasing Zr content from 0.00 to 0.10, the main peaks shift towards lower angle, indicating that the Zr^{4+} ions get substituted in the BFO lattice and induce structural

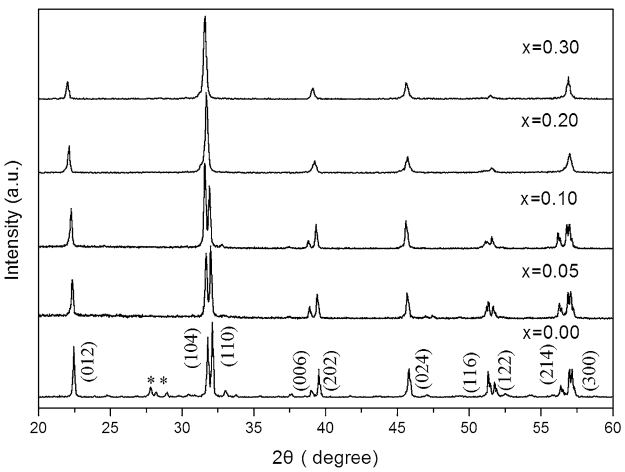

Fig. 1 XRD patterns of $BiFe_{1-x}Zr_xO_3$ ceramics at room temperature

distortion. At the same time, peak merging at the vicinity of 32° and decrease in the intensity of some peaks (~ 38°, 51° and 57°) in the $x = 0.20$ and 0.30 samples reveal that a structure transition happens. This phenomenon may be attributed to the mismatch of ionic radii between Zr^{4+} (0.72 Å) and Fe^{3+} (0.645 Å) [12].

The SEM images of all the samples are illustrated in Fig. 2. It can be seen that with increasing Zr^{4+} concentration, the morphologies of the samples change significantly. The morphology of the undoped BFO is non-uniform, the shape of grains is irregular, and a large amount of pores exist at the inter and intra grains. The pores exist in some large grains on the fracture due to that rapid grain growth resulting from the formation of a liquid phase occurred during the sintering process. With Zr doping, the grain size distribution becomes more uniform and the microstructures becomes denser. It

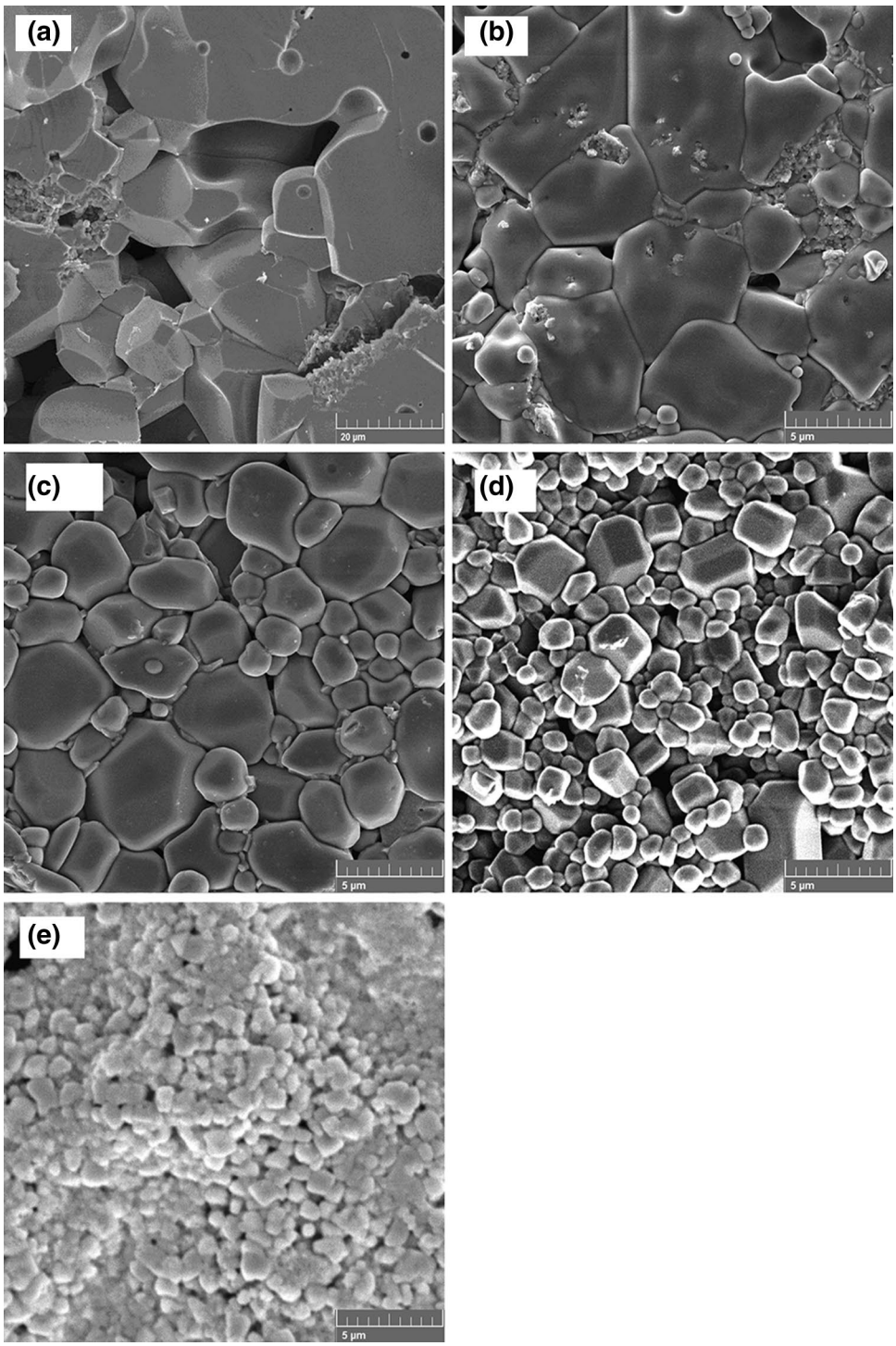

Fig. 2 SEM images of $BiFe_{1-x}Zr_xO_3$ samples **a** $x = 0$, **b** $x = 0.05$, **c** $x = 0.10$, **d** $x = 0.20$ and **e** $x = 0.30$

is also found in Fig. 2 (b–e) that the average grain size is remarkably decreased with increasing Zr content, indicating that the Zr doping hinders the grain growth. The substitution of Zr^{4+} for Fe^{3+} requires charge compensation which can be achieved by filling the oxygen vacancies. The decrease in grain size with increasing Zr concentration may be due to the suppression of oxygen vacancies which hampers the migration of oxygen ions and consequently reduces grain growth rate. And the decrease of grain size may also due to the slower diffusion of Zr^{4+} ion [7], which has bigger ionic radius than Fe^{3+} ion.

A detailed study of the microstructural defects in the $BiFe_{1-x}Zr_xO_3$ ceramics was performed by positron lifetime measurements. Three positron lifetime components τ_1, τ_2 and τ_3, and the corresponding intensities I_1, I_2 and I_3 ($I_1+I_2+I_3=1$) can be extracted from the lifetime spectra after source correction. Among these components, the longest component τ_3 can be ignored in our following discussion due to its low intensity ($I_3<0.7\%$). And the data of positron annihilation are analyzed with two components after normalizing I_1 and I_2 again.

According to the two-state trapping model, the bulk lifetime annihilated from a perfect lattice can be denoted as $\tau_b = 1/(I_1/\tau_1 + I_2/\tau_2)$, which is supposed to probe the intrinsic properties of lattice [25, 28]. The long positron life time τ_2 and the corresponding intensity I_2 are supposed to reflect the size and the concentration of the cation vacancy-type defect, respectively [28]. The average lifetime τ_m can be calculated by the following equation:

$$\tau_m = \tau_1 I_1 + \tau_2 I_2 \quad (1)$$

which has a universal stability and reliability. τ_m can primarily reflect the annihilation process in the delocalized free state and the trapped state, and give the detail of electron density and defect distribution inside the materials [28]. Figure 3 presents the positron lifetime components τ_m and τ_2 in $BiFe_{1-x}Zr_xO_3$ ceramics as a function of Zr content x. It can be seen that τ_m increases slightly with increasing x from 0.00 to 0.10, while increases rapidly when x increases from 0.10 to 0.20, and then increases weakly as $x>0.20$. These reflect that the Zr doping causes a decrease of electron density at the annihilation sites included in vacancy-like defects and perfect lattice, which can be considered as the changes of chemical surroundings in annihilation sites. And τ_m increases drastically at $x=0.20$ indicates that a structural transition occurs. The long lifetime τ_2 shown in Fig. 3 increases monotonically with increasing Zr content from 0.00 to 0.30. And τ_2 is directly proportional to the size of vacancy-type defect [28]. This means that the size of vacancy-type defect increases with increasing Zr content in the range of 0.00–0.30, probably induced by the agglomeration of vacancy clusters. Figure 4 shows the long positron lifetime intensity I_2 as a function of Zr content x. It can be found that I_2 increases at Zr content x from 0.00 to 0.20, and then decreases slightly from 0.20 to 0.30, indicating that the cation vacancy concentration increases firstly and then decreases with increasing Zr content. The valence of Zr^{4+} ion is higher than that of Fe^{3+} ion, the substitution of Zr^{4+} ions for Fe^{3+} ions at B-site requires charge compensation by creation of negatively charged Fe^{3+} vacancies ($V_{Fe}^{'''}$), which should be a trap of positron, as described by the following equation:

$$3ZrO_2 \rightarrow 3Zr_{Fe}^{\bullet} + V_{Fe}^{'''} + 6O_O^x \quad (2)$$

where $Zr_{Fe}^{\bullet}$ is Zr ion with +1 effective charge at Fe site. Therefore, Zr substitution in the BFO is expected to create the Fe vacancies, and the vacancy concentration increases with increasing x from 0.00 to 0.20. And the slight decrease

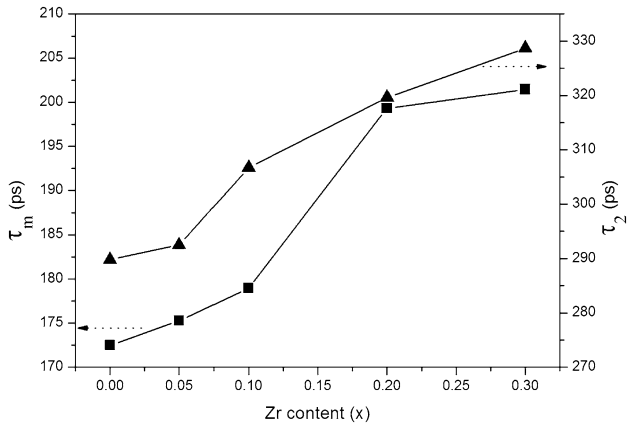

Fig. 3 Positron lifetime τ_m and τ_2 of $BiFe_{1-x}Zr_xO_3$ samples as a function of Zr content x

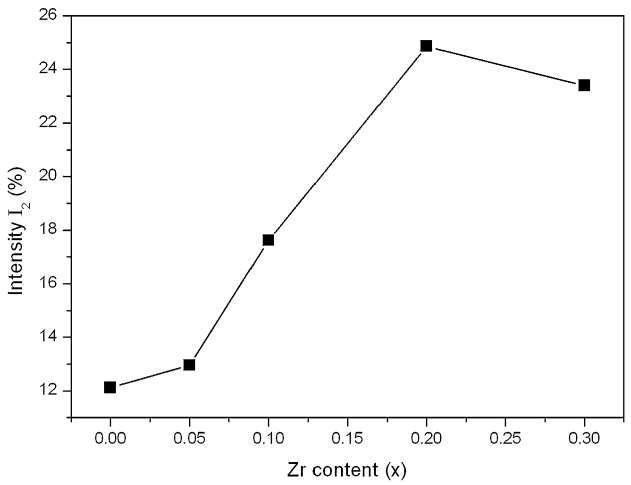

Fig. 4 Intensity I_2 of $BiFe_{1-x}Zr_xO_3$ samples as a function of Zr content x

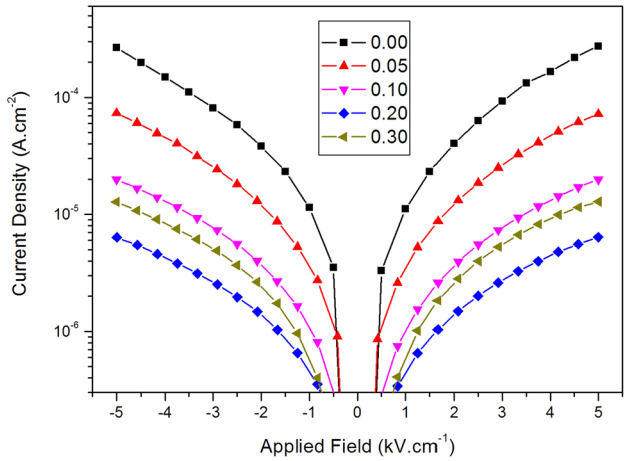

Fig. 5 Leakage current density versus applied electric field (*J–E*) of $BiFe_{1-x}Zr_xO_3$ samples

of I_2 for $x=0.30$ sample may imply that the defect concentration becomes gradually saturation.

Figure 5 illustrates leakage current density versus electric field (*J–E*) characteristics of $BiFe_{1-x}Zr_xO_3$ ceramics measured at room temperature. The increase in current density with applied electric field is nonlinear suggesting non-ohmic characteristics of the prepared samples. It can be clearly seen that the undoped BFO exhibits a relatively high leakage current density, while the Zr doped BFO samples have lower leakage current densities. This clearly reveals that the leakage current density can be effectively reduced by Zr doping. Under an applied electric field of 5 kV/cm, the leakage current densities of the undoped BFO, $BiFe_{0.95}Zr_{0.05}O_3$, $BiFe_{0.9}Zr_{0.1}O_3$, $BiFe_{0.8}Zr_{0.2}O_3$ and $BiFe_{0.7}Zr_{0.3}O_3$ are about 2.75×10^{-4}, 7.22×10^{-5}, 1.98×10^{-5}, 6.38×10^{-6} and 1.28×10^{-5} A/cm^2, respectively. It means that the leakage current density decreases with increasing Zr content *x* from 0.00 to 0.20, and then increases at *x* from 0.20 to 0.30. As is well known, the large leakage current density in BFO mainly results from oxygen vacancies and valence fluctuation of iron ions (Fe^{3+}–Fe^{2+}). The oxygen vacancies are the trapping centers for electrons and the electrons trapped in them can be readily activated by the applied electric field, leading to the increase of leakage current density [29]. The hopping of electrons from Fe^{2+} to Fe^{3+} is also contributed to electronic conduction when oxygen vacancies are present as a "bridge" between Fe^{2+} and Fe^{3+} in the lattice. And it is found that such a phenomenon plays an important role in electronic conduction [29, 30]. It is apparent in comparison with Figs. 5 and 4 that the leakage current density and vacancy defect concentration I_2 show an opposite change tendency. It may be concluded that the cation vacancy defect is one of the most import factors which can affect the leakage current of BFO. The Fe vacancy with negative charge created by Zr doping will decrease the negative charge induced by valence fluctuation of iron ions (Fe^{3+}–Fe^{2+}), to reach electric neutrality [31]. In this way, the amount of Fe^{2+} is decreased; hence, the electron hopping between Fe^{3+} and Fe^{2+} is suppressed by Zr doping. Another reason for the improved leakage current property with increasing *x* from 0.00 to 0.20 is due to the decrease of oxygen vacancies. The electronegativity values of Zr, Fe, Bi and O ions are 1.33, 1.83, 2.02 and 3.44, respectively [32]. Therefore, the bond strength of Zr-O bond is higher than both the Fe–O and Bi–O bonds. Zr addition into BFO leads to a reduction in oxygen vacancy concentration due to stronger Zr–O bond. And the Zr^{4+} ions play a role of donor in BFO because the valance of Zr^{4+} is higher than that of Fe^{3+} ions, and charge imbalance can be compensated by filling the oxygen vacancies [13]. The third reason may be that Zr doping reduces the grain sizes of $BiFe_{1-x}Zr_xO_3$ ceramics, resulting in an increase in the leakage current pathways and the density of grain boundary, which can make a contribution to the decrease in leakage current density [9]. In addition, the suppressing the formation of impurity phases is also beneficial to decrease the leakage current density of $BiFe_{1-x}Zr_xO_3$ ceramics.

Figure 6 shows the room temperature *P–E* loops for $BiFe_{1-x}Zr_xO_3$ ceramics. All the samples show unsaturated *P–E* curves due to high leakage current. Compared with undoped BFO, a significant improvement of the ferroelectric properties can be observed in the Zr doped samples. The remanent polarization (*Pr*) is about 0.003, 0.026, 0.452, 0.320 and 0.173 uC/cm^2 for $x=0.00$, 0.05, 0.10, 0.20 and 0.30 samples, respectively. It indicates that the remanent polarization increases with increasing Zr concentration from 0.00 to 0.10, and then decreases with further increasing *x*. The large leakage current of undoped BFO makes it difficult to obtain good ferroelectric properties. From Fig. 5, it can be found that the leakage current density decreases

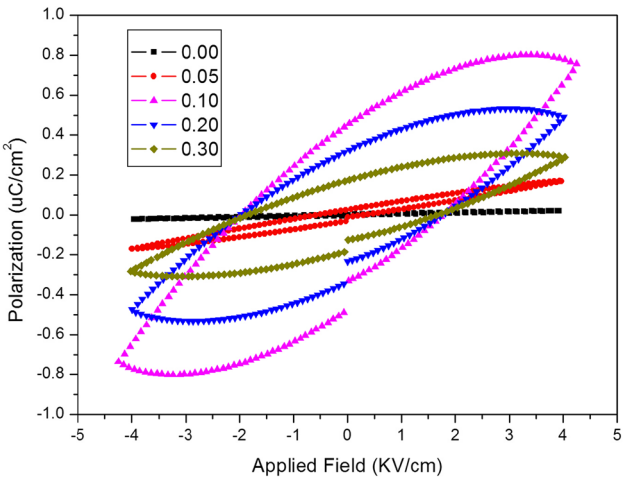

Fig. 6 Ferroelectric hysteresis (*P–E*) loops of $BiFe_{1-x}Zr_xO_3$ ceramics at room temperature

with increasing Zr content from 0.00 to 0.10. Therefore, the ferroelectric properties increase with increasing Zr content from 0.00 to 0.10. Another reason is the suppressed oxygen vacancy concentrations induced by higher-valent Zr^{4+} doping, as oxygen vacancies can play a critical role in the pinning of polarization switching domains [33]. Oxygen vacancies usually accumulate near domain boundaries, hence can cause domain pinning and reduce the *P*r value of the ferroelectrics. However, since the radius of Zr^{4+} ion is larger than that of Fe^{3+} ions, the incorporation of Zr^{4+} ion is expected to obtain smaller rattle space than Fe^{3+} in the oxygen octahedron and this would lead to a decrease in polarization [33]. Therefore, the ferroelectric properties decrease with the increase of Zr content from 0.10 to 0.30. The other reason is the decreased grain size with increasing Zr content. As is known that the strength of polarization is strongly related to the grain size [34], a decrease in grain sizes can result a reduced polarization.

Figure 7 shows the magnetic hysteresis (*M*–*H*) loops of the $BiFe_{1-x}Zr_xO_3$ ceramics measured at room temperature with a maximum magnetic field of 70 kOe. Magnetization has been found to be increased with increasing applied magnetic field for all samples. The undoped BFO exhibits a linear magnetic field dependence of the magnetization, which indicates the antiferromagnetic nature [30]. However, the weak ferromagnetic nature is observed in Zr doped samples [29]. It means that the antiferromagnetism of BFO could be turned into weak ferromagnetism by Zr doping. The remanent magnetization (*M*r) is about 0.043, 0.063, 0.123 and 0.086 emu/g for $x = 0.05$, 0.10, 0.20 and 0.30 samples, respectively. It indicates that the Mr increases with increasing Zr content from 0.00 to 0.20, and thereafter decreases with further increasing Zr doping content ($x > 0.20$). By comparing Fig. 7 with Fig. 4, it can be found that the magnetic properties and vacancy defect concentration I_2 have a same change tendency. It could be deduced that the magnetic properties seem related to the cation vacancy defect concentration in $BiFe_{1-x}Zr_xO_3$ ceramics, and the Fe vacancy defect is one of the most import factors which can tailor the magnetic properties of BFO. Actually, the improved magnetism in BFO based ceramic originates from the suppression of the space-modulated antiferromagnetic spin orderings as mentioned in other papers [27, 29, 30]. Upon the substitution of magnetic Fe^{3+} ions by nonmagnetic Zr^{4+} ions, the Fe vacancies are created due to the requiring of charge compensation so that the nearest antiparallel spin orderings of Fe^{3+} ions in lattice are broken by the Fe vacancies [13]. This is the non-cancellation among spin orderings that leads to a net magnetic moment. The other reasons for the significant increase in remanent magnetization of the $BiFe_{1-x}Zr_xO_3$ may be as follows: (1) The insertion of nonmagnetically active Zr^{4+} ions in antiferromagnetic Fe sublattice perturbs the spiral spin modulation and thus destroys the spiral. This results in release of the latent magnetization locked within structure, and enhances the magnetic moment. (2) The structural distortion and transition induced by Zr doping in BFO lattice changes the bond length and bond angle, suppresses and even destructs the spatial spin modulation, resulting in enhanced magnetization in $BiFe_{1-x}Zr_xO_3$ [27, 29, 30].

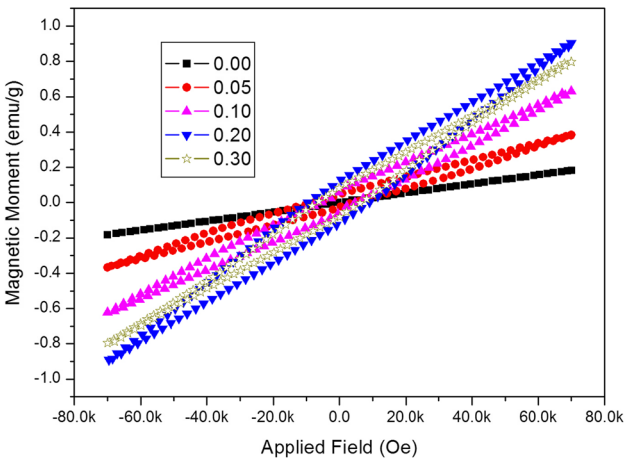

Fig. 7 Magnetization hysteresis (*M*–*H*) loops of $BiFe_{1-x}Zr_xO_3$ ceramics at $T = 300$ K

4 Conclusions

In summary, multiferroic $BiFe_{1-x}Zr_xO_3$ ($x = 0.00$–0.30) ceramics were synthesized using solid state reaction method followed by rapid liquid phase sintering. The microstructure, electrical and magnetic properties of synthesized samples were investigated. Single phase formation of the Zr doped samples is identified by XRD, and a structure phase transition with increasing the Zr doping content is observed. The SEM images show that the grain size of Zr doped BFO obviously decreases with the increase of Zr concentration, and the grain size distribution becomes uniform. The PAS studies indicate that cation vacancy-type defects are present in the all samples, and the size of cation vacancy-type defect increases with increasing Zr content. The cation vacancy concentration increases with increasing Zr content from 0.00 to 0.20, and then decreases with further increase of Zr content. Electric measurements show that Zr doping can effectively improve the leakage and ferroelectric properties, and the doping content affect significantly the leakage current and ferroelectricity of BFO ceramics. Magnetic measurements indicate ferromagnetism in Zr doped BFO ceramics. The remanent magnetization increases with increasing the Zr content from 0.00 to 0.20, while decreases with further increase of Zr content. The vacancy defect concentration has an opposite change tendency with leakage current density, while has a same change tendency with magnetic properties.

It could be concluded that the cation vacancy defect is one of the most import factors which can modulate the electric and magnetic behaviors of BFO.

Acknowledgements This work is supported by the National Natural Science Foundation of China (No. 11775192, 11305142, 11675149), National Natural Science and Henan Province United Foundation of China (No.U1204601) and Key Members of the Outstanding Young Teacher of Henan Province and Zhengzhou University of Light Industry (No. 2015GGJS-185).

References

1. J. Ma, J.M. Hu, Z. Li, C.M. Nan, Adv. Mater. **23**, 1062 (2011)
2. W. Eerenstein, N.D. Mathur, J.F. Scott, Nature **442**, 759 (2006)
3. G.H. Jaffari, A. Samad, A.M. Iqbal, S. Hussain, A. Mumtaz, M.S. Awan, M. Siddique, S.I. Shah, J. Alloys Compd. **644**, 893 (2015)
4. G.F. Cheng, Y.J. Ruan, W. Liu, X.S. Wu, Phys. B **468–469**, 81 (2015)
5. P.C. Sati, M. Arora, S. Chauhan, S. Chhoker, M. Kumar, J. Appl. Phys. **112**, 094102 (2012)
6. K. Kalantari, I. Sterianou, S. Karimi, M.C. Ferrarelli, S. Miao, D.C. Sinclair, I.M. Reaney, Adv. Funct. Mater. **21**, 3737 (2011)
7. A.F. Hegab, I.S. Ahmed Farag, A.M. EL Shabiny, A.M. Nassaar, A.A. Ramadan, A.M. Moustafa, J. Mater. Sci. **28**, 14460 (2017)
8. Y. Ma, W.Y. Xing, J.Y. Chen, Y.L. Bai, S.F. Zhao, H. Zhang, Appl. Phys. A **122**, 63 (2016)
9. A. Sathiya Priya, I.B. Shameem Banu, Z. Mohammed, J. Mater. Sci. **28**, 8467 (2017)
10. C.M. Raghavan, D. Do, J.W. Kim, W.J. Kim, S.S. Kim, J. Am. Ceram. Soc. **95**, 1933 (2012)
11. K.S. Kumar, J. Ayyappan, C. Venkateswaran, Mater. Res. Bull. **65**, 224 (2015)
12. M. Arora, S. Chauhan, P.C. Sati, M. Kumar, S. Chhoker, R.K. Kotnala, J. Mater. Sci. **25**, 4286 (2014)
13. X. Qi, J. Dho, R. Tomov, M.G. Blamire, J.L. MacManus-Driscoll, Appl. Phys. Lett. **86**, 062903 (2005)
14. J.J. Xie, C.D. Feng, X.H. Pan, Y. Liu, Ceram. Int. **40**, 703 (2014)
15. T. Matsui, E. Taketani, H. Tsuda, N. Fujimura, K. Morii, Appl. Phys. Lett. **86**, 082902 (2005)
16. S. Mukherjee, R. Gupta, A. Garg, V. Bansal, S. Bhargava, J. Appl. Phys **107**, 123535 (2010)
17. J. Wei, R. Haumont, R. Jarrier, P. Berhtet, B. Dkhil, Appl. Phys. Lett. **96**, 102509 (2010)
18. J. Wei, D.S. Xue, Appl. Surf. Sci. **258**, 1373 (2011)
19. M. Arora, S. Chauhan, P.C. Sati, M. Kumar, J. Supercond. Nov. Magn. **27**, 1867 (2014)
20. D.J. Keeble, R.A. Mackie, W. Egger, B. Lowe, P. Pikart, C. Hugenschmidt, T.J. Jackson, Phys. Rev. B **81**, 064102 (2010)
21. J.H. Hadley, F.H. Hsu, E.R. Vance, B.D. Beggw, J. Am. Ceram. Soc. **88**, 246 (2005)
22. M. Latkowska, M. Baranowski, W.M. Linhart, F. Janiaka, J. Misiewicz, N. Segercrantz, F. Tuomisto, Q. Zhuang, A. Krier, R. Kudrawiec, J. Phys. D **49**, 115105 (2016)
23. G. Panzarasa, S. Aghion, G. Soliveri, G. Consolati, R. Ferragut, Nanotechnology **27**, 02LT03 (2016)
24. L. Sedivy, J. Cizek, E. Belas, R. Grill, O. Melikhova, Sci. Rep. **6**, 20641 (2016)
25. H.F. He, X.F. Li, Z.Q. Chen, Y. Zheng, D.W. Yang, X.F. Tang, J. Phys. Chem. C **118**, 22389 (2014)
26. P. Banerjee, A. Franco Jr., J. Mater. Sci. **27**, 6053 (2016)
27. C.A. Wang, H.Z. Pang, A.H. Zhang, X.B. Lu, X.S. Gao, M. Zeng, J.M. Liu, Mater. Res. Bull. **70**, 595 (2015)
28. T. Li, J. Chen, D.W. Liu, Z.X. Zhang, Z.P. Chen, Z.X. Li, X.Z. Cao, B.Y. Wang, Ceram. Int. **40**, 9061 (2014)
29. M. Muneeswaran, R. Dhanalakshmi, N.V. Giridharan, Ceram. Int. **41**, 8511 (2015)
30. S. Zhang, L. Wang, Y. Chen, D. Wang, Y. Yao, Y. Ma, J. Appl. Phys. **111**, 074105 (2012)
31. Y.H. Gu, Y. Wang, F. Chen, H.L.W. Chan, W.P. Chen, J. Appl. Phys. **108**, 094112 (2010)
32. P.C. Juan, C.L. Sun, C.H. Liu, C.L. Lin, F.C. Mong, J.H. Huang, H.S. Chang, Microelectron. Eng. **109**, 142 (2013)
33. Y. Li, J. Yu, J. Li, C. Zheng, Y. Wu, Y. Zhao, M. Wang, Y. Wang, J. Mater. Sci. **22**, 323 (2011)
34. X.Z. Wang, H.R. Liu, B.W. Yan, J. Eur. Ceram. Soc. **29**, 1183 (2009)